Novel diamond shuttle to deliver flexible bioelectronics with reduced tissue compression

Kyounghwan Na[1], Zachariah J. Sperry[2,3], Jiaao Lu[1], Mihaly Vöröslakos[1,4], Saman S. Parizi[1], Tim M. Bruns[2,3], Euisik Yoon[1,2], John P. Seymour[1]*

Affiliations

[1]Electrical Engineering & Computer Science Department, University of Michigan, Ann Arbor, MI, USA

[2]Biomedical Engineering Department, University of Michigan, Ann Arbor, MI, USA

[3]Biointerfaces Institute, University of Michigan, Ann Arbor, MI, USA

[4]The Neuroscience Institute, New York University, New York, NY, USA

Abstract

The ability to deliver flexible biosensors through the toughest membranes of the central and peripheral nervous system is an important challenge in neuroscience and neural engineering. Bioelectronic devices implanted through dura mater and thick epineurium would ideally create minimal compression and acute damage as they reach the neurons of interest. We demonstrate that a three-dimensional diamond shuttle can be easily made with a vertical support to deliver ultra-compliant polymer microelectrodes (4.5 µm thick) in-vivo through dura mater and thick epineurium. The diamond shuttle has 54% less cross-sectional area than an equivalently stiff silicon shuttle, which we simulated will result in a 37% reduction in blood vessel damage. We also discovered that higher frequency oscillation of the shuttle (200 Hz) significantly reduced tissue compression regardless of the insertion speed, while slow speeds also independently reduced tissue compression. Insertion and recording performance are demonstrated in rat and feline models, but the large design space of these tools are suitable for research in a variety of animal models and nervous system targets.

27

28 ## 1 Introduction

29 Implantable sensor arrays, especially when deployed in neural mapping studies, are most accurate
30 and insightful when damage and disruption to nervous system circuitry is minimized. Minimizing
31 damage and reactivity has been emphasized by recent global initiatives including the BRAIN Initiative,
32 the NIH SPARC program, the GSK Innovation Challenge, and several DARPA funding programs, which
33 have supported the development of new technology for mapping, monitoring, and/or controlling the
34 nervous system with higher fidelity and longevity. Previous work demonstrated that size of an implant
35 effects the neuron count and several glia markers of reactivity[1,2]. A precise implant size to tissue damage
36 function is still missing, but evidence suggests that care should be taken to minimize the damage to blood
37 vessels which densely permeate nervous tissue[3,4]. Central nervous system (CNS) neurons, for example,
38 are located within ~15 μm of a capillary vessel[5–7] so damage to the blood-brain barrier is unavoidable.
39 When designing an implantable device, the penetrating structure must be stiff enough to reach the desired
40 target with accuracy and, more challenging, piercing a tough fibrous outer membrane protecting the neurons.
41 These challenges have opposing solutions – make the device as fine as possible for minimal bleeding and
42 cellular disruption, yet ensure it is sufficiently stiff so as not to buckle or move off-target during
43 penetration. The challenge is underscored when the covering membrane, the epineurium or dura mater in
44 the peripheral or central nervous systems respectively, is left intact during insertion.

45 Epineurium and dura mater are made of collagen fibers interspersed with elastin and fibroblasts
46 that are at once tough and flexible[8,9]. Cranial and spinal dura mater have a Young's modulus in the range
47 of 2-100 MPa[10] (depending on species and location) and so compared to the parenchyma, whose modulus
48 is ˜5 kPa, provide the primary resistance to device insertion. In the feline dorsal root ganglia (DRG), the
49 epineurial thickness is in the range of 20-100 micrometers (typically 80μm)[11]. The dura can often be

separated with minimal damage to the parenchyma below with surgical training and skill, however the creation of dural flaps severs blood vessels extending into brain and allows the brain to swell and dehydrate [4]. Furthermore, surgically removing the epineurium at the DRG or further into the periphery is not done in practice without damaging the nervous tissue. As such, a minimally invasive solution to penetrating through CNS and peripheral nervous system (PNS) membranes is needed.

State-of-the-art sensor arrays have taken different approaches to the problem of penetration when the membrane cannot be removed. One high-density and popular electrophysiology research tool is the "Utah" array[12,13], which is a silicon array comprised of many ~70 μm diameter needles. It is inserted with a pneumatic insertion tool and can achieve an insertion velocity of 12 m/s[14]. The array has a wide base so it naturally stops when fully inserted but also may induce significant compression or impact trauma. No published quantification of the insertion force and compression distance exists, but significant bleeding has been reported[15,16]. Potentially related to this issue, the histology clearly shows encapsulation around the shank tips[15,17,18] with a typical electrode-tip to axon distance of 40 to 150 μm. The resulting tissue restructuring around these microelectrodes prevents high-fidelity chronic recording, although it is still effective in recording population-based compound action potentials and for electrical stimulation[19]. Another popular recording/stimulation array, but with a smaller footprint and greater electrode density, are planar silicon probes. Historically these have been called "Michigan" arrays but these micromachined silicon structures are now made by many groups[20–24] and companies. They are typically inserted in the CNS using a manual manipulator at a moderate speed so as to monitor for buckling during insertion. Given the risk of buckling or fracture, silicon planar probes are rarely used to penetrate tough membranes and there is even less known about the insertion mechanics. One study also demonstrated there is a chronic breach in the blood-brain-barrier for rigid intracortical structures [25].

New research has been focused on implanting flexible arrays with assistance from a variety of

73 techniques. Given the impressive flexibility and stretchability of nerves, ganglia, and the spinal cord,
74 researchers have attempted to insert flexible forms of microelectrodes. The most common insertion
75 techniques are pulling the array through the tissue using thread and needle, a dissolvable stiffener, or a
76 removable shuttle, otherwise known as a stylet. Several groups have demonstrated the pull-through
77 technique for intrafascicular recording used a fine commercial needle and suture[26,27]. The diameter of
78 these suture needles are hundreds of microns and risk causing significant trauma. As Wurth, et. al,
79 carefully demonstrated in their histology the electrode to axon distance is typically 100 microns or more
80 over time[27]. A dissolvable stiffener comes at the cost of greater volume given the temporary material is
81 several orders of magnitude less stiff than many inorganics[28,29], let alone the potential reactivity induced
82 by the degraded polymer itself. The shuttle or stylet approach [2,30–33] allows for stiffer materials and thus a
83 smaller footprint than commercial needles or organic stiffeners. However, none of those approaches
84 would allow for insertion through a tougher membrane without making the substrate much larger and at
85 the cost a significantly more tissue damage.

86 **Our approach**

87 This paper seeks to address the combined insertion challenge of minimizing the cross-sectional
88 area and the tissue compression. This work adds to previous research using a shuttle approach but
89 having a unique T-shaped geometry and material to form a three-dimensional ultrananocrystalline
90 diamond (UNCD) shuttle with 13-fold greater stiffness than a similar cross-section made with
91 conventional silicon (Fig. 1b). UNCD has the highest modulus of elasticity (800-1000 GPa)[34,35] of any
92 conformal thin-film and 5X and 3X higher than silicon[32,33] and carbon[30]. We demonstrate a simple 2-
93 mask method of fabrication (Fig. 1c). We also describe a biological model of blood vessel damage that
94 others can use to predict damage from any arbitrary geometry. We also quantify the insertion dynamics
95 in phantom and various tissues. Finally, we use the shuttle to demonstrate the delivery of and neural

recordings from an ultra-compliant polyimide array (Fig. 1a). We expect this new ability to deliver higher-density bioelectronics with less compression and less vascular damage will improve the understanding of CNS and PNS function.

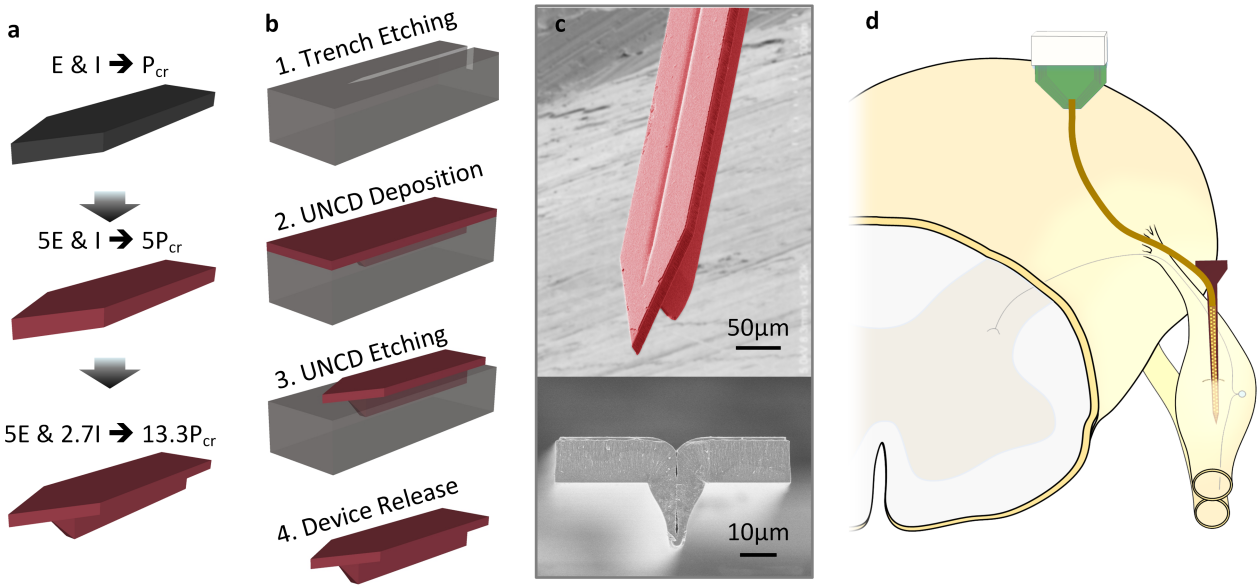

Fig 1. | Insertion concept, design concept, and fabrication of a ultra-nano-crystalline diamond (UNCD) shuttle. a, Progression of design improvement from a simple silicon shuttle, with a buckling load of P_{cr}, to an improvement of $13.3*P_{cr}$ by changing the Young's Modulus, E, and moment of inertia, I. **b,** Process flow of UNCD shuttle. **c,** SEM of released UNCD shuttle. **d,** Insertion of flexible electrode array into a dorsal root ganglia (DRG) using a rigid shuttle and retraction.

2 Results

Blood vessel damage model

While a reduction of area potentially leads to diminution of insertion damage to tissue, we have no biological evidence that this rule is still valid for T-shaped geometry. To address this, we modeled the damage using an available model of the density, size, and length of micro-vascular segments in the brain[6,7]. A three-dimensional micro-vascular network data for rat brain is publicly available.[36] We overlaid the contour of a variety of devices onto the microvasculature maps provided initially by scanning electron microscope (SEM) imaging and 3D reconstruction. The model assumes that the device contour damages any vessel for which there is contact. This approach allows us to assess the

114 performance of T-shape geometry in terms of a quantitative analysis of blood vessel invasion. The
115 numbers of micro-vascular segments cut by the footprints of the shanks were counted throughout 1,000
116 insertion iterations with randomized angles and locations for two equivalently rigid geometries (Fig 2).
117 The chosen T-beam cross-section contour was 11 x 65 µm on the planar portion and a vertical support
118 that was 27.5µm-deep that tapered from 16 to 2µm-wide. This T-shaped UNCD (T-UNCD) was used
119 for this model and throughout the study. The silicon device that has an equivalent buckling strength is
120 34-µm thick. All devices in this study are 65-µm wide which is generally the accepted width of a
121 minimally damaging brain probe for chronic recording[23,37]. On average the simulation produced a
122 36.6% reduction in blood vessel damage caused by the T-UNCD relative to the Si-34 rectangular silicon
123 device. Two important points of reference are a 15-µm thick silicon probe, which is sufficient for
124 insertion in rodent models with the dura removed, and another commercially available neural probe that
125 is 50-µm thick and intended for larger animal models. We compare these two against a T-UNCD
126 structure that has equivalent stiffness with Si-15 (T-UNCD SMALL) and is considerably smaller in
127 area. The simulation results were 1.4 vessels damaged compared to 5.8 vessels damaged by Si-15. By
128 contrast, the 65x50-µm geometry caused damage that was 9.7-fold greater than the smaller T-UNCD
129 (Supp. Fig. 2).

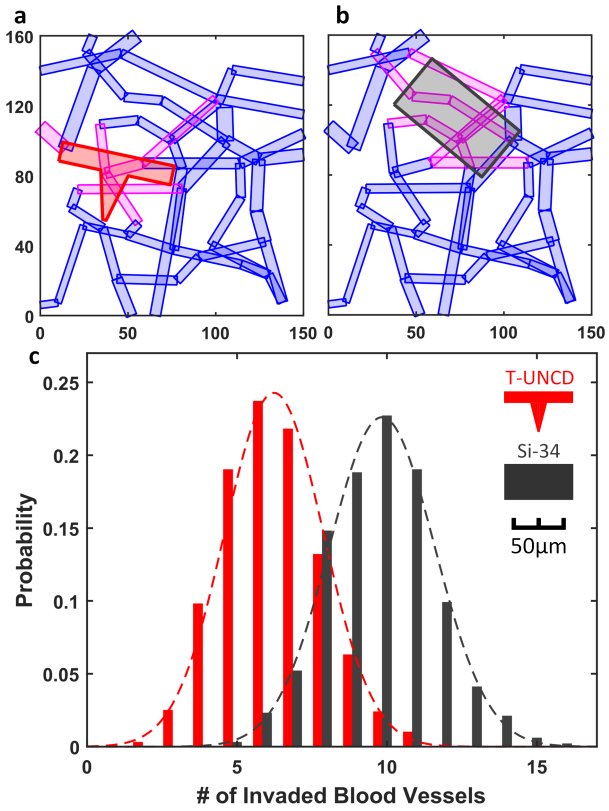

Fig 2. | Simulation result of blood vessel invasion comparing Si (dark gray) and T-UNCD (red) having an identical buckling strength. Examples of invasion analysis with **a,** T shape with 65µm by 11µm on the planar portion and 27.5µm-deep, 16µm to 2µm-wide trapezoid for the vertical support, which has identical buckling strength with (b). **b,** 65µm by 34µm rectangle. **c,** Simulation result of 1,000 insertions yielded a Gaussian distribution of the number of invaded blood vessels. Mean values of two geometries from (a-b) were 6.23 and 9.84, respectively. Invaded blood vessels in (a-b) indicated in magenta. X and Y labels in (a-b) indicated the coordinates in µm.

Creating 3-D UNCD structures

The diamond T-beam shape was successfully created by patterning a tapered trench into silicon and then filling it with a moderately conformal UNCD diamond. The conformality of UNCD deposition is related to the sticking coefficient and varies in a large range according to the deposition condition and the species involved[38]. Our specific conditions and sticking coefficient were unknown because the hot filament chemical vapor deposition method used for this work was provided by an outside vendor and the details were proprietary. We developed a method to model the deposition profile and estimate the sticking coefficient during deposition. This was critical for defining the proper silicon trench profile (Fig. 1c) and thus minimize void creation in the shuttle's vertical support. Our deposition model (Supp.

146 Note 1) fit best (R^2>0.94) with a sticking coefficient, η_0 = 0.079. The void formed was less than 0.4 μm
147 across because of the trench's taper angle of 70˚. The angle of the silicon trench can be modified for
148 deeper or wider geometries in the future by combining different doses of isotropic and anisotropic dry
149 etching.

150 **Buckling load calculations & measurements**

151 The most dominant mechanism of mechanical failure for insertion of a needle-shaped device is
152 due to buckling. An insertion will end up with a failure when the buckling load is lower than the
153 required insertion force. In this case, the shank keeps deflecting more without a load increase and
154 breaks eventually when the deflection-induced stress exceeds the fracture strength of the material.
155 Buckling loads for 15μm-thick planar Si (Si-15), 50μm-thick planar Si (Si-50), 11μm-thick planar
156 UNCD (P-UNCD) and T-shaped UNCD (T-UNCD) shanks were measured (Fig. 3a). The
157 characterization of buckling load was essential to analyze the results of insertion testing. Another goal
158 of the buckling load measurement is the validation of the elastic modulus of UNCD and its structural
159 design. The buckling loads of Si-15 and Si-50 were measured as -8.4% and +11.3% of the calculated
160 value (Fig. 3a). The buckling load was calculated by equation (1) as:

161 $$P_{cr} = \frac{\pi^2 EI}{(KL)^2} \quad (1)$$

162 where E is Young's modulus, I is the moment of inertia, K is the effective length factor, and L is the
163 length. The K value is dependent on the boundary condition and it is assumed as a fixed-pinned
164 condition in which K=0.699 but as discussed later is not always true. For consistency, all shuttles were
165 also 1.5-mm long unless otherwise stated.

166 The variation of thickness affects the buckling load significantly because the moment of inertia is
167 proportional to the cubic of thickness. The range of UNCD's Young's modulus has been reported as

880-1000 GPa[34,39,40] and our estimated value based on our known geometry best fit to 800 GPa. The measured buckling load of P-UNCD was 2.3% lower than that of the calculation, and it implies that the estimation for Young's modulus is reasonable. The measurement of T-UNCD buckling load was 15.5% lower than the calculation and this is most likely due to the imperfection of the trench filling and the remaining void.

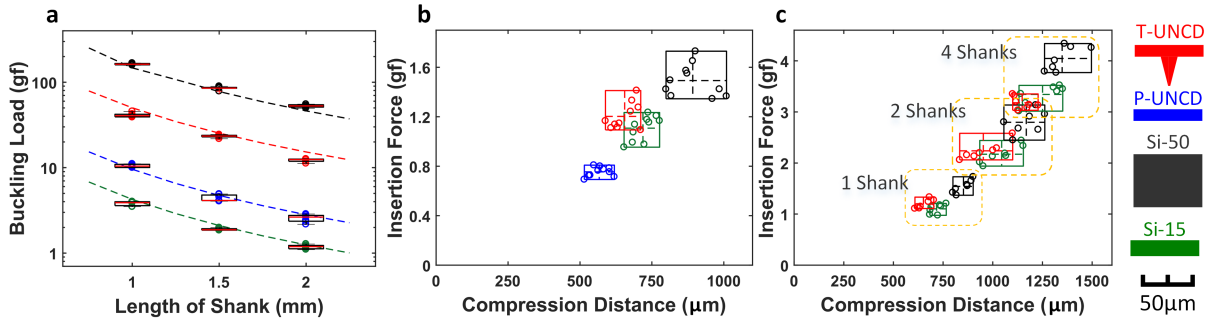

Fig 3. | Mechanical characterization of various shuttles in a tissue phantom. a, Buckling load according to material, geometries and lengths, including two silicon geometries that are commercially available, N=7. **b,** Insertion force of single shank shuttles, N=10. **c,** Insertion force of 1, 2 and 4 shanks for three different probes, N=7 (planar diamond not tested). For 4-shanks, the force per shank was 0.8, 0.84, and 1.0 gf for T-UNCD, Si-15, and Si-50, respectively. The inter-shank spacing was 250 µm. Insertion speed was 0.01 mm/s in all cases.

Insertion force in phantom and feline DRG

Ex vivo tissue has a limited shelf life so many tests were conducted using a 100-µm thick PDMS sheet (Sylgard 184), to simulate dura and epinuerium, secured over a larger volume of agar gel. Our experiments showed that this phantom was stiffer than rat dura and almost as stiff as feline DRG epineurium (Table 1). Sylgard 184 (1-2 MPa)[41] and agar have similar moduli as dura[10] and parenchyma[42,43]. The chisel-shaped tips for all variations of shuttles had identical angles and the thickness varied based on film thickness, which was chosen because it is the standard tip of all Michigan-style probes.

Table 1. Average Peak Insertion Force [A]

Needle	T-UNCD				Pulled pipette[B]	
Tissue	Rat dura	Phantom	Cat DRG	Cat[C] dura	Rat dura	Phantom
Force, g	0.68±0.22 N=6	1.2±0.1 N=10	1.9±0.7 N=6	1.4±0.2 N=2	0.40±0.03 N=2	1.7±0.2 N=8

Note A: Oscillation force data could not be collected
Note B: 2-µm diameter tip
Note C: Lumbo-sacral region of spinal cord

A typical force response is an increasing force during the initial insertion until an abrupt drop indicating a puncture event. This force-distance pattern of one or more punctures in soft-tissue is well-documented[44]. It was expected that the thinner tip required less insertion force than thicker geometries as was actually observed (Fig. 3b), though it was not linear. T-UNCD consistently showed multiple puncture events indicated by two force peaks. This corresponds to the tips of horizontal part and the vertical part of T-shape, respectively (Supp. Fig. 3b). The first peak force occurred at the range of P-UNCD insertion forces (0.75 g) and the second occurred following a further increase of force. The average peak insertion force for this T-UNCD was 1.2 gf and was 8.7% higher than Si-15 (Fig. 3b).

The insertion force of 1, 2 and 4 shanks for each cohort were compared to investigate the behavior of multi-shank insertion (Fig. 3c). Multiple shanks were 250 µm center-to-center from an adjacent shank. The force versus compression results, regardless of material and geometry, were less than a linear sum. Similarly, a three-dimensional assembly of six 4-shank UNCD arrays resulted in a decreasing force when normalized per shank (Supp. Fig. 4).

Ex vivo insertion tests with explanted feline L6, L7, and S1 DRG were conducted to evaluate the feasibility of epineurium penetration. The average insertion forces required for successful penetration of P-UNCD, Si-15, T-UNCD, and Si-50 were 1.15 ± 0.28, 0.96 ± 0.32, 1.92 ± 0.69 and 2.76 ± 0.61 gf,

respectively (Fig. 4). However, Si-15 had the most failures (9 failures in 15 trials) followed by P-UNCD (4 failures in 19 trials), with no failures observed for the other two geometries. Our results indicate that T-UNCD will penetrate the feline epineurium with 100% success like Si-50 but with only about half of the cross-sectional area. P-UNCD and Si-15 will not reliably penetrate. In a qualitative *in vivo* test, the same T-UNCD design penetrated feline spinal cord (lumbar-sacral levels) nine times with zero failures where the dura is expected to be even thicker.

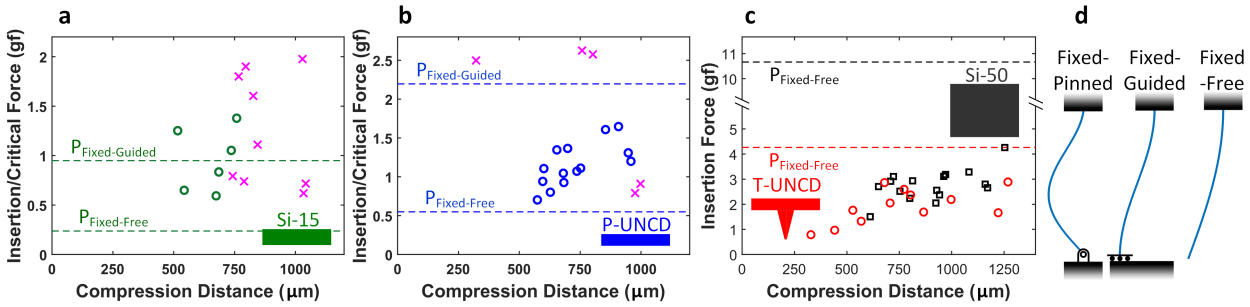

Fig 4. | Result of ex-vivo insertions into cat DRG. a, 15µm-thick Si. "x" marks an insertion failure. **b,** 11µm-thick planar UNCD. **c,** T-shaped UNCD and 50µm-thick Si. **d,** Generic boundary conditions for the buckling load calculation (K=0.699, K=1, and K=2 respectively). The probe backend, at top, is fixed in each scenario and tissue is at the bottom. Theoretical limits noted as dashed lines in (a, b, c).

Mechanical dynamics of insertion: speed and oscillation

In an effort to better understand the effect of linear speed and high-speed oscillation we modified our previous force sensor experiments. A piezoelectric motor capable of uniaxial movement with an amplitude of up to 70 µm was mounted onto a linear motor. A macro lens and video camera were also added to collect high-resolution compression information (Supp. Fig. 3c). Both linear speed and oscillation frequency were varied and the maximum compression distance (taken from annotated video images) was measured for each condition (N=6; Fig. 5). We found the greatest compression was 328 µm and occurred at 22 mm/s, linear motion only. At the other extreme, the compression was 124 µm at 0.01 mm/s and an oscillation of 200 Hz. This is a relative reduction of 62%. A graph of position and velocity over time for several tested motor parameters are provided (Supp. Fig. 6). A side-by-side video comparison of the UNCD shuttle at 0.01 mm/s with and without oscillation is also provided (Supp. Video

2).

Oscillation frequencies of 10 and 100 Hz were tested at 2 mm/s and a similar trend was observed with increasing frequency, which lowered the magnitude and variance of the compression (p=0.087, Supp. Fig 5). We also achieved a significant reduction of compression with a pipette (2-µm tip diameter) with 200 Hz oscillation (p=0.0007, Supp. Fig. 7).

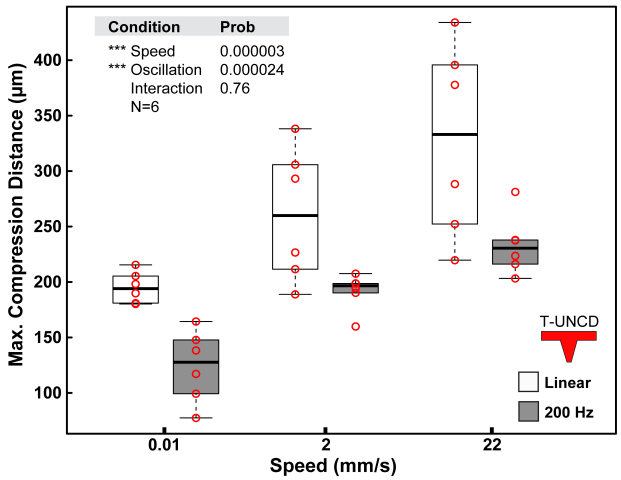

Fig 5. | Result of T-UNCD phantom insertion with and without oscillation according to insertion speed. ANOVA results with an interaction term included. Both speed and oscillation were significant but the interaction term was not. Values for the maximum compression distance were taken from video analysis.

In vivo demonstration in feline DRG and spinal cord

The T-UNCD shuttle was inserted into the S1 or S2 DRG of three separate felines at 1.3 mm/s without oscillation. One animal had mechanical testing performed, which also included successful shuttle penetrations through the spinal cord dura (Table 1). In the other two animals, functional arrays were mounted on the T-UNCD shuttles (Fig. 6) and successfully recorded neural activity. Evoked activity was recorded from a variety of stimulus types across the span of the array, including cutaneous neurons from unique locations in the perineal region and base of the tail (Fig. 7). In the first experiment, a total of 28 different channels had a unit out of 42 functional channels, spanning 1 mm in depth across the array. We observed 7 putative units on subsets of these 28 channels, which were overlapping due to the closeness of the electrodes (40-µm pitch). In the second animal experiment, we observed approximately 40 putative

units out of 48 channels spanning 1.06 mm in depth when the probe was in a fixed position. When the same probe was retracted, neural activity was observed on all 59 functional channels, including one putative bladder afferent (not shown). As described further in Supp. Note 3, in the second experiment we observed amplitudes greater than 1 mV and the median peak-to-peak amplitude for all experimental trials was 91 μV.

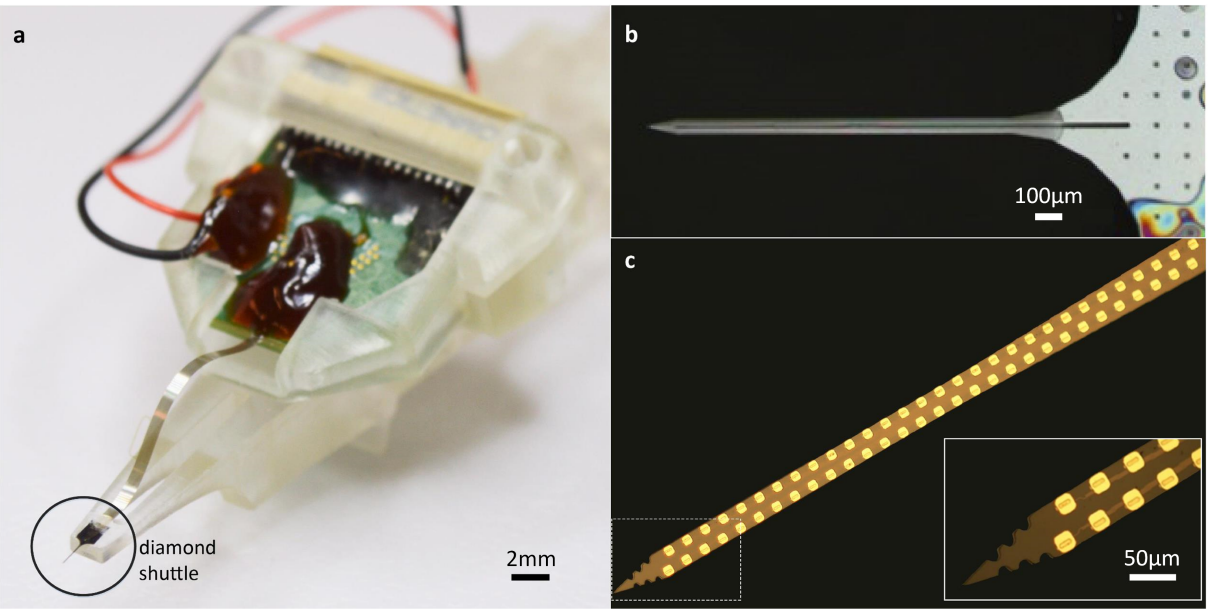

Fig 6. | Assembly of high density flexible array mounted on UNCD shuttle. a, Photograph of entire assembly including the flexible polyimide array mounted on a UNCD shuttle. PCB is secured by a removable jacket that slides in a track of the shuttle jig. The insertion motor (not shown) is connected to the 3D printed shuttle jig. **b,** Top view of PEG-coated UNCD shuttle. **c,** Polyimide-based flexible array with 60 recording sites and (inset) zoomed view of the array tip.

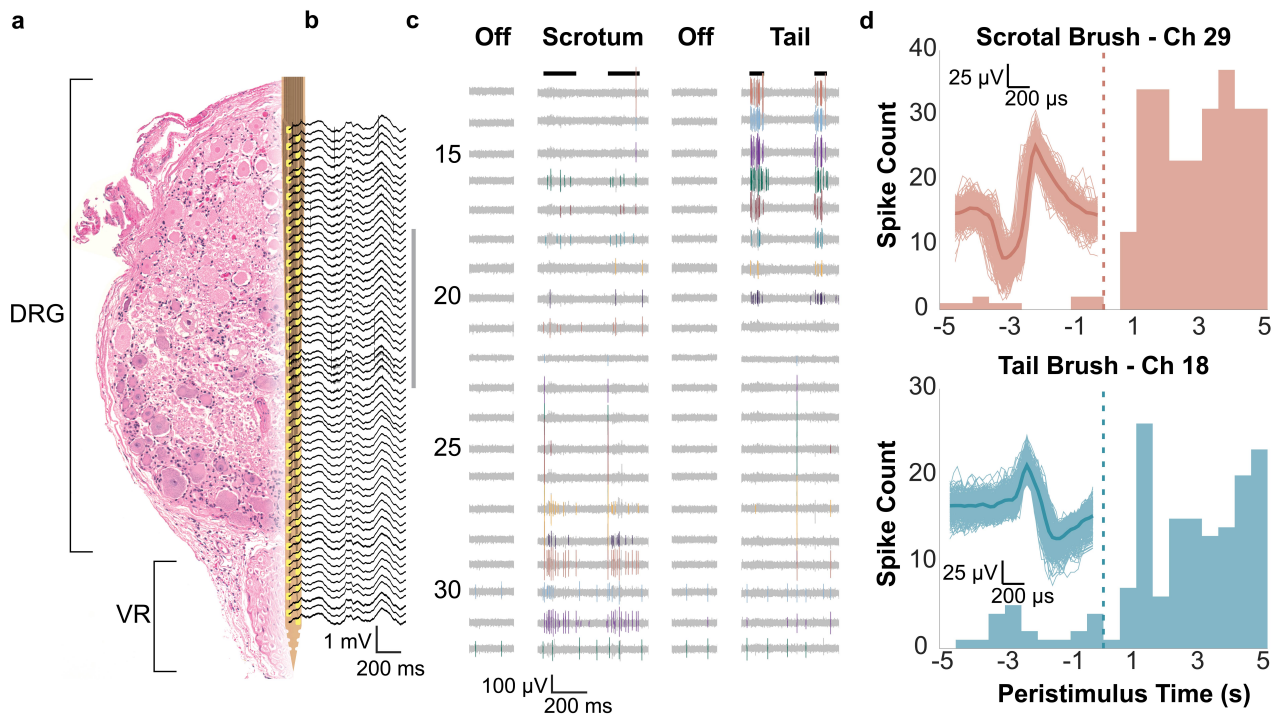

Fig 7. | Recorded neural signals from feline sacral DRG for evoked stimuli. a, Diagram of the array in DRG. On the left is a representative hematoxylin and eosin stained cross-section of an example DRG with the ventral root (VR) below. Overlaid is a CAD diagram of the array, with array sites in yellow. The array and DRG are to scale. **b,** Wideband signal (highpass filter with 2 Hz cutoff) recorded during scrotum brushing. **c,** High pass filtered signals recorded during two sensory input trials (scrotum and tail brush strokes indicated by black lines at top). Channels shown are indicated by the gray vertical line to the right of (b). Manually sorted single units are in color. **d,** Peri-stimulus time histograms (PSTHs) for two channels and trial types, labeled and colored by channel numbers shown in (c). For both units shown, brushing starts at 0 s and continues through 5 s, including multiple individual strokes. Overlaid on each PSTH are the corresponding spike waveforms, with the mean waveform given as a dark thick line of the same color.

In vivo demonstration in rat brain

We inserted the T-UNCD shuttle into the motor cortex through dura mater at 0.01 mm/s with and without oscillation (N=6) without fracture or failure. The depth of insertion was 1.5 mm. Without oscillation, the compression was 642 µm, and with 200 Hz oscillation the compression was 488 µm, a reduction of 24% (p=0.25, t-test). Separately, we also inserted the T-UNCD – polymer device through dura mater of anesthetized rats (2 insertions in each of 2 rats) also without failure. The flexible electrode was attached to the T-UNCD in the same way as in the feline surgery. After successful insertion the probe was separated from the UNCD shuttle (Supp. Video 3) and wideband (0.3 Hz – 3000 Hz) and single unit neuronal activity were recorded from the somatosensory cortex of the rat (N=1, Supp. Fig. 9a

300 and b). The spontaneous neuronal activity was recorded for 30 minutes and 20 putative single units were
301 found (Supp. Fig. 9).
302
303 **3 Discussion**
304 We demonstrated that in rat and feline models of dura and thick epineurium, our novel T-beam
305 UNCD shuttle can deliver a thin, flexible high-density microelectrode array that would be especially
306 useful in neural mapping studies. The reduced-footprint with high stiffness features of the shuttle
307 exhibited better insertion features in tissue analogues and *ex vivo* neural tissue than standard probes.
308 There are also many design opportunities for thicker or thinner UNCD shuttles whose thickness,
309 including the vertical support, can be in the range of 5 to 52 μm, which is potentially translated into the
310 range of buckling load up to 102 gf. As we demonstrate in our results, important considerations like the
311 boundary condition of a buckling model are especially important in the periphery. We also compare this
312 shuttle approach to others.
313 **Buckling model highly dependent on boundary conditions**
314 Throughout the *ex vivo* insertion tests with explanted feline DRG, many trials for Si-15 and P-
315 UNCD resulted in failures (Fig. 4a, b) even though this was not expected based on the standard
316 assumption of a probe tip "pinned" to stationary tissue (Fig. 4d). This commonly cited condition, where
317 K = 0.699, may work for rodent brain implants but was incorrect for our *ex vivo* DRG experiments. Our
318 results implied that the boundary condition at the contact between the tip and the tissue varied across
319 trials presumably due to a varying angle of contact, the shape and curvature of the targeting tissue, and
320 the friction of the tip at the surface. Also, that is a probable situation for *in vivo* insertion into peripheral
321 nerve which will have similar variations. Adding to that risk is the breathing artifact observed in larger
322 animal models. In these situations, the boundary condition is expected to be somewhere between fixed-

323 guided (where the tip is pinned sufficiently to the tissue but the tissue itself rotates or moves;example
324 failure in Supp. Video 1) or fixed-free (where the tip does not remain embedded in the surface and free to
325 slip). This latter case is most likely due to a large insertion angle, which is challenging to avoid on highly
326 curved surfaces. Also, a duller tip will not pin as effectively as a sharp one. The *ex vivo* insertion results
327 suggested that it would be safe and wise to design the mechanics of a shuttle based on the worst-case
328 boundary condition, especially when inserted into the PNS. This means the structure should be 8X stiffer
329 than one designed for the fixed-pinned condition.

330 **Advantages of T-UNCD over other shuttle approaches**

331 Mounting a polymer array on the shuttle and the separation after insertion is an important,
332 practical issue for a successful *in vivo* experiment. Fortunately, a planar polymer array will self-align on a
333 planar shuttle due to geometrical similarity and surface tension when dipped in a solution of water or
334 polyethylene glycol. This may be a simpler approach than using a cylinder-shaped shuttle, e.g. tungsten
335 wire or carbon wire[30,31] where the fabrication is expensive and does not scale to multi-shank devices.
336 Also the resulting cross-section is a rectangle tangent to a circle and thus creating more damage than
337 either alone. T-UNCD has the advantages of both stiffness and a matching geometry for the high-density
338 polymer arrays used here and by other groups [26,27,33]. Also, compared to the stylet approach, the planar
339 shuttle is more appropriate to deliver multi-shank electrodes readily enabling higher channel count.
340 Furthermore the T-UNCD forms a sharp tip that is effectively notched to create a micropost. Luan et. al
341 demonstrated the micropost but this version required focused ion beam etching which is slow and costly
342 compared to large-scale microfabrication. Nonetheless the micropost concept is advantageous if the
343 immediate release of a device is critical in an application and the potential of bending the polymer tip is
344 not a concern. Future work may use the T-UNCD as a micropost in order to speed the release after
345 insertion in feline DRG experiments where breathing movement was significant. In the above acute

346 recording demonstration, the shuttle remained for almost an hour at a time and in each case the shuttle
347 was broken from breathing movements. When the shuttle was removed within 5 minutes of implant, the
348 shuttle was intact, but releasing the biosensor array within 5 minutes using polyethylene glycol was not
349 possible in our experience. Thus the micropost approach with the UNCD would be ideal for chronic
350 recordings in large animals with significant tissue movement.

351 We believe that T-UNCD is superior to other shuttles even when a large insertion force is not
352 required (e.g., when dura mater is removed). Assuming 6mm length of a shank, buckling loads of T-
353 UNCD SMALL and Si-15 are estimated as 0.19 gf and 0.16 gf, and the former reduces the blood vessel
354 damage to 24% of the latter (Supp. Fig. 2). T-UNCD SMALL has 37% less cross-sectional area than
355 20μm-diameter tungsten wire which has an estimated buckling load of 0.18gf.

356 **Insertion dynamics with oscillation**

357 The tissue compression in some scenarios was clearly visible, especially in feline *ex vivo* DRG
358 samples where the small size of the ganglion underscored the surface movement (Fig. 4 and Supp. Video
359 1). Previous work in rats, albeit without an intact dura, demonstrated that low speed reduced force and
360 tissue compression at a speed as low as 0.2 mm/s[45]. Therefore, our evident tissue compression at a much
361 lower speed of 0.01 mm/s prompted further investigation beyond speed. The ability to reduce insertion
362 force and compression with oscillations has been documented in mosquitos[46] and demonstrated with a
363 small needle attached to a vibratory actuator with a kilohertz frequency[47]. In the former case, slow
364 oscillations of up to 15 Hz using a three-part cutting system make a fascinating but complicated
365 micromachine. In the latter case, the oscillations were 600 μm in amplitude and lateral to the direction of
366 insertion. While this reduced both compression and the insertion force, this risks damage to the nervous
367 tissue. To address this, we employed a piezo stage with motion only in the direction of penetration and
368 tested for the first time the combination of speed and frequency.

To study this required an accurate measure of compression. Initially, the experiments only collected force versus position data with low resolution video recording. In those experiments we could not measure the maximum compression distance but only the total distance the probe moved before the peak force was observed. This over-estimates the compression distance since slow or small rupture events occurred before a larger rupture event, as others have reported[45,48]. Later we added video recording and a stabilized 4X macro lens (Supp. Fig. 3c). From this the maximum compression (Fig. 5 and Supp. Fig. 5) could be more accurately measured with annotated video images and on-screen measurements.

For some time, some neuroscientists have used slow-speed insertion for its perceived reduction in dimpling and tissue strain[49]. Our data confirms that slow speed, independent from oscillations, reduced the compression distance even in the context of a tougher membrane. Interestingly, high-frequency oscillation creates higher speed but in this case also significantly reduced compression and variability. The kinematics of the movement is straightforward to model (Supp. Fig. 6) and the maximum instantaneous speed and acceleration is calculated in Supp. Table 1. Given that the components of the insertion force includes the compression force (non-linear spring model), friction, and cutting forces[44], a more careful study should be conducted to isolate the effect of speed and oscillation on each. Further research should also measure the acute damage to the blood-brain-barrier[4,25,50] over this range of motion. Until more is known about the effect of oscillation on the vascular system, the best strategy would be to simply turn off oscillation after the initial rupture event is detected.

4 Outlook

High-density bioelectronics for the nervous system have a long way to progress before we achieve biomimetic scale, equivalent tissue mechanics, and effectively no tissue-reactivity but the modeling and materials work shown here is an important step in that direction. The results presented here demonstrate

392 the highest-density and most flexible polymer array to date—60 traces and 65-µm wide on a substrate
393 only 4.5-µm thick—inserted through the toughest nervous system tissues to obtain neural signals. We
394 have developed a versatile T-shaped ultrananocrystalline diamond shuttle which provides a 56%
395 reduction in cross-sectional area compared to a planar silicon shuttle with equivalent insertion strength,
396 and still stiff enough to insert into different neural structures in small and medium animal models with the
397 dura and epineurium intact. This same structure will theoretically reduce micro-vascular damage by 37%
398 compared to standard probes. We also quantified the benefits of slow insertion and demonstrated for the
399 first time the use of uni-directional oscillation. This oscillation significantly reduced phantom tissue
400 compression by 31%, showing the potential for limiting neural tissue impact for *in vivo* use. More
401 broadly, the use and deployment of advanced bioelectronics as developed here is critical for high-
402 resolution scientific research into the nervous system and will contribute to future clinical devices in the
403 treatment of neurological damage and disorders.
404
405
406 **5 Methods**
407 **Blood-vessel damage model**
408 A publicly available three-dimensional micro-vascular network data for rat brain[6,7,36] was used to
409 simulate the blood vessel invasion induced by the insertions of various geometries. For simplicity, the 3-
410 D model was projected into a 2-D plane assuming that the insertion was vertical and straight. 1,000
411 insertion simulations were conducted per geometry and the inserted geometry was randomly located in
412 terms of x, y locations and rotation per trial. A segment of blood vessel was classified as damaged when a
413 device crossed the entire width of a segment. The distribution of the number of damaged blood vessels
414 was fit to a Gaussian distribution to extract the mean value and the deviation.

415 **UNCD fabrication**

416 The process flow is illustrated in Fig. 1c. First, standard photolithography defined a trench pattern
417 on a 4" silicon wafer. A tapered trench was formed on silicon wafer by the combination of DRIE and
418 isotropic dry etching. Smooth sidewalls were achieved by thermal oxidation and removal followed by
419 another thermal oxidation for sacrificial layer growth. Afterward, 11-µm thick UNCD film was deposited
420 by hot filament chemical vapor deposition (CVD) at Advanced Diamond Technologies, Inc. (Romeoville,
421 IL). Then, 2 µm-thick plasma-enhanced CVD silicon dioxide was deposited at 350˚C to be used as a hard
422 mask for UNCD etching. Following photolithography, silicon dioxide and UNCD were dry-etched
423 sequentially using C_4F_8 and O_2 chemistries, respectively. The UNCD-only devices were released in
424 buffered hydrofluoric acid by soaking for 6 hours and carefully rinsed with deionized water. A
425 deposition model of UNCD in a trench is described in Supp. Note 1.

426 **Mechanical characterization**

427 The inital setup for mechanical characterization was built using a precision load cell (Model 31,
428 Honeywell, 50 g maximum), a digital multimeter (34011A, Agilent) and a motorized translation stage
429 (MTS50-Z8, Thorlabs). This setup was used for data collected in Fig. 3, 4, and Supp. Fig. 4 and
430 illustrated in Supp. Fig 3a. For the oscillation and speed studies (Fig. 5, Supp. Fig. 5 and Supp. Fig. 7) we
431 used a piezostage HS1.70 from Piezoconcept (Lyon, France) mounted on the linear motor. The
432 piezomotor was driven by a function generator where a 10V sine input produced a 70-µm PP amplitude.
433 The silicon or UNCD shuttle was fixed to the end of load cell and the voltage output of the load cell was
434 recorded through the ADC (225 samples per sec.) while the stage transfers the counterpart. The exerted
435 force and travel distance were calculated by conversion of recorded data. The velocity and acceleration of
436 the linear motor were 0.01 mm/s and 0.1 mm/s^2 respectively.

437 A tissue phantom was formed by a 100µm-thick Sylgard 184 sheet secured over 0.7% agar gel.

438 The *ex vivo* DRG and spinal cord tissues were used within 72 hours of extraction from felines used for
439 other research purposes. All samples were kept in saline and continually rehydrated during an experiment
440 to minimize mechanical degeneration or stiffening of tissues.

441 The recorded videos and the force-distance plots were used for the failure criteria of *ex vivo* DRG
442 insertion. An insertion trial was classified as a failure when buckling was obvious from the video. In such
443 cases, it was also evident in the force plot as there was no rupture event, i.e. drop in force over time. In
444 other cases the shuttle fractured due to large bending.

445 **Maximum compression distance measurement**

446 To capture more precise compression data during oscillation we used a Canon ES Rebel 5 with a
447 macro lens (MP-E Macro 65mm 1:2.8) set to 4X zoom mounted on an optical bench (Supp. Fig. 3c). The
448 insertion process was recorded over the full length of penetration, 1.5 mm. These videos were then
449 analyzed in Photoshop. Initially a line marking the point of contact was annotated over the video, then a
450 second line was added at the point of maximum compression. A pixel to pixel measurement was made in
451 Photoshop and converted to distance. The pixel to distance ratio used in these videos was identical for all
452 and determined by the known width of the shuttle (65 μm). The angle between the camera lens and
453 phantom surface was measured (within 1 degree) and used to correct for the final maximum compression
454 value; the average angle was 7 degrees.

455 **Polymer array fabrication**

456 A flexible electrode array was fabricated broadly as we and others have described[31,51]. One layer
457 of 2.2 μm-thick polyimide (PI-2610 from HD Microsystems) was spin-coated on a sacrificial layer and
458 fully cured at 350˚C. This thin, biostable PI is BPDA-PDA (3,3′,4,4′-biphenyltetracarboxilic dianhydride
459 with p-phenylene diamine)[52]. This variety of polyimide was chosen because of its high yield strength,
460 flexibility, and low water absorption[53]. Metal patterning was formed in several steps depending on

461 resolution requirements. 500-nm lines at 65-nm thickness were formed using a GCA stepper i-line
462 lithography tool. This high resolution enabled 60 traces at a maximum width of 70 µm. Future work
463 could also employ multi-layer metal. Wider and thicker metal was patterned using a Seuss MA-6 contact
464 aligner over the interconnects and bond pads. A TiO_2 adhesion layer above and below metal traces was
465 used to presumably improve adhesion, although not yet validated. The top PI-2010 layer was also 2.5-µm
466 thick. The PI was etched by oxygen plasma to define the shape and open the electrical contact sites.
467 Ti/Au electrode metal was patterned by a liftoff process and devices were released by the removal of the
468 sacrificial layer. The electrode pitch was 40 µm. In order to decrease the impedance of the recording
469 electrode sites, PEDOT-pTS was coated on Au electrodes as described elsewhere[54]. The impedance in
470 PBS was lowered to 24.0 ±1.45 kΩ from 1.98±0.752 MΩ of Au electrode (Supp. Fig. 8).

471 **Mounting polymer array on UNCD shuttle**

472 The ultra-flexible electrode array was electrically assembled on a PCB and then mechanically
473 assembled on a UNCD shuttle for *in vivo* insertion and recording. First, the PI arrays were ball bonded
474 onto a printed circuit board[55] and the assembly was placed into a 3D-printed jacket designed to slide in
475 the track of a shuttle jig (Fig. 6a). Separately, a UNCD shuttle was aligned and mounted on a 3D-printed
476 shuttle jig followed by dip coating into a beaker of PEG (12,000 MW) heated to 70-90°C (Fig. 6b). The
477 PI array assembly was roughly aligned over the shuttle, aligning the vertical position by sliding the array
478 assembly in its track on the jig. This position was then fixed to the shuttle backend by a small drop of
479 PEG (4,000 MW). Precise self-alignment was achieved by once again dip-coating in heated PEG (12,000
480 MW). The resulting film was again 1 to 2 µm thick and transparent. This self-alignment achieved an
481 accuracy of at least 5-µm.

482 ***In vivo* experiment, feline DRG**

483 Procedures were performed in three adult, intact felines (male, 4.6-6.1 kg). Neural recordings

484 were performed in two animals while only insertion testing was performed in a third. All steps were
485 approved by the University of Michigan Institutional Animal Care and Use Committee (IACUC; protocol
486 PRO00007296). As described elsewhere[51], felines were sedated with a ketamine-butorphanol-
487 dexmedetomidine intramuscular dose prior to intubation and maintenance under isoflurane anesthesia (2-
488 4%) with an intravenous saline drip (5-10 mL/kg/hr) and vitals monitored and maintained within normal
489 ranges. A laminectomy was performed to expose the lumbosacral (~L7-S3) DRG. Bone screws were
490 inserted into the iliac crests bilaterally. The feline was placed into a custom testing stand[56] which
491 supported the chest. Stainless steel wire was wrapped around each iliac crest bone screw and fixed to the
492 stand, allowing for the lower abdomen and hind limbs to be suspended. This positioning reduced the
493 relative motion due to breathing that would occur at the DRG. A jig holding a shuttle-mounted array was
494 attached to a linear inserter (M-230.25, Physik Instrumente, Karlsruhe, Germany) mounted on a
495 micromanipulator (KITE-R, World Precision Instruments, Sarasota, FL, USA), which was used to
496 position the array just above a DRG (S1 or S2). The inserter was driven at a rate of 1.3 mm/s to insert the
497 array and shuttle to a depth of 1.4 mm through the DRG. A variety of sensory stimuli were applied to
498 activate sensory neurons, including brushing of different cutaneous dermatomes related to the DRG
499 implanted (scrotum, anus, base of tail), infusion of saline into the bladder, and skin-surface electrical
500 stimulation. Neural signals were sampled at 30 kHz with a Neural Interface Processor (Grapevine,
501 Ripple, Salt Lake City, Utah, USA). After an experiment neural signals were first sorted in Offline Sorter
502 (Plexon, Dallas, TX, USA) prior to analysis with custom scripts in MATLAB (Mathworks, Nantick, MA,
503 USA).

504 ***In vivo* experiment, rat dura**

505 The experiment was approved by the Institutional Animal Care and Use Committee at the University of
506 Michigan (protocol number: PRO00007275). Two male wistar rats (600 g) were implanted with a

507 UNCD-polyimide electrode under isoflurane anesthesia (1.2 – 1.5%). No prior experimentation had been
508 performed on this rat. Atropine (0.05 mg/kg, s.c.) was administered after anesthesia induction to reduce
509 saliva production, and the rectal temperature was monitored and kept constant at 36–37 °C with a DC
510 temperature controller (TCAT-LV; Physitemp, Clifton, NJ, USA). Proper depth of anesthesia was
511 maintained by confirming the lack of nociceptive reflex. A craniotomy was drilled (4 by 4 mm), carefully
512 paying attention to not damage the dura mater. The hole was cleaned and filled with sterile saline solution
513 (0.9%, MWI, USA) and kept wet until the custom-electrode was implanted at 1 mm posterior from
514 bregma and 2.8 mm lateral of the midline, in the S1FL area of the somatosensory cortex.

515 The electrode was inserted to a 2 mm depth in the cortex using the custom motor system (0.01
516 m/s, 200 Hz oscillation, Supp. Fig. 3c). The insertion/dura penetration process was video recorded
517 (Canon ES Rebel 5 camera was attached to a Zeiss OPMI-1 microscope, 31.25x total magnification). In
518 one of the rats, the separation process was initiated by applying sterile saline on the array ten minutes
519 after insertion. Once the upper part of the polyimide was separated the UNCD shuttle was slowly moved
520 (50 μm up and down) until a complete separation was visible under microscope. Then, the shuttle was
521 retracted while the recording electrode was kept in place (Supp. Video 3). The recorded signals (n = 60
522 channels) were amplified (200X gain) and stored after digitization at 20 kHz sampling rate per channel
523 (RHD2132 and RHD2000 Evaluation System, Intan Technologies, Los Angeles, CA).

524 The recorded data were analyzed by custom-written scripts in MATLAB (MathWorks, USA).
525 Neuronal spikes were detected from the digitally high-pass filtered signals (0.5–3 kHz) by Spikedetekt2
526 (https://github.com/klusta-team/spikedetekt2). Detected spikes were automatically sorted using
527 KlustaKwik2[57], followed by manual adjustment of the clusters using KlustaViewa software[58] to get well-
528 isolated single units (multi-unit and noise clusters were discarded).

529

Acknowledgments

The authors thank the staff of the Lurie Nanofabrication Facility for their tool support and technical advice when needed. We thank Paras Patel for his help in PEDOT-pTS coating. We also thank Ahmad Jiman, Zhonghua Aileen Ouyang, and Lauren Zimmerman for their help in 3D printing materials for and/or data collection in feline experiments. This work was supported in part by the National Institute of Biomedical Imaging and Bioengineering of the National Institutes of Health (R21EB020811, and SPARC program Awards U18EB021760, OT2OD024907, and OT2OD023873), and Seed Funding for Innovative Projects in Neuroscience from the University of Michigan Brain Initiative Working Group (MiBrain). The content is solely the responsibility of the authors and does not necessarily represent the official views of the National Institutes of Health or the University of Michigan.

References

1. Seymour, J. P. & Kipke, D. R. Neural probe design for reduced tissue encapsulation in CNS. *Biomaterials* **28,** 3594–3607 (2007).
2. Kozai, T. D. Y. & Kipke, D. R. Insertion shuttle with carboxyl terminated self-assembled monolayer coatings for implanting flexible polymer neural probes in the brain. *J. Neurosci. Methods* **184,** 199–205 (2009).
3. Salatino, J. W., Ludwig, K. A., Kozai, T. D. Y. & Purcell, E. K. Glial Responses to Implanted Electrodes in the Brain. *Nat. Biomed. Eng.* **1,** 862–877 (2017).
4. Kozai, T. D. Y. *et al.* Reduction of neurovascular damage resulting from microelectrode insertion into the cerebral cortex using in vivo two-photon mapping. *J. Neural Eng.* **7,** 46011 (2010).
5. Tsai, P. S. *et al.* Correlations of neuronal and microvascular densities in murine cortex revealed by direct counting and colocalization of nuclei and vessels. *J. Neurosci.* **29,** 14553–14570 (2009).
6. Motti, E. D., Imhof, H. G. & Yaşargil, M. G. The terminal vascular bed in the superficial cortex of the rat. An SEM study of corrosion casts. *J. Neurosurg.* **65,** 834–846 (1986).
7. Secomb, T. W., Hsu, R., Beamer, N. B. & Coull, B. M. Theoretical simulation of oxygen transport to brain by networks of microvessels: effects of oxygen supply and demand on tissue hypoxia. *Microcirculation* **7,** 237–247 (2000).
8. Weerasuriya, A. & Mizisin, A. P. in *The Blood-Brain and Other Neural Barriers* 149–173 (Springer, 2011).
9. Thomas, P. K. The connective tissue of peripheral nerve: an electron microscope study. *J. Anat.* **97,** 35–44 (1963).
10. Maikos, J. T., Elias, R. A. I. & Shreiber, D. I. Mechanical properties of dura mater from the rat

brain and spinal cord. *J. Neurotrauma* **25,** 38–51 (2008).
11. Ostrowski, A. K., Sperry, Z. J., Kulik, G. & Bruns, T. M. Quantitative models of feline lumbosacral dorsal root ganglia neuronal cell density. *J. Neurosci. Methods* **290,** 116–124 (2017).
12. Nordhausen, C. T., Rousche, P. J. & Normann, R. A. Optimizing recording capabilities of the Utah intracortical electrode array. *Brain Res.* **637,** 27–36 (1994).
13. Wark, H. A. C. *et al.* A new high-density (25 electrodes/mm2) penetrating microelectrode array for recording and stimulating sub-millimeter neuroanatomical structures. *J. Neural Eng.* **10,** 45003 (2013).
14. Rousche, P. J. & Normann, R. A. A method for pneumatically inserting an array of penetrating electrodes into cortical tissue. *Ann. Biomed. Eng.* **20,** 413–422 (1992).
15. Branner, A., Stein, R. B., Fernandez, E., Aoyagi, Y. & Normann, R. A. Long-term stimulation and recording with a penetrating microelectrode array in cat sciatic nerve. *IEEE Trans. Biomed. Eng.* **51,** 146–157 (2004).
16. Christensen, M. B. *et al.* The foreign body response to the Utah Slant Electrode Array in the cat sciatic nerve. *Acta Biomater.* **10,** 4650–4660 (2014).
17. Wark, H. A. C., Mathews, K. S., Normann, R. A. & Fernandez, E. Behavioral and cellular consequences of high-electrode count Utah Arrays chronically implanted in rat sciatic nerve. *J. Neural Eng.* **11,** 046027 (2014).
18. McCreery, D., Cogan, S., Kane, S. & Pikov, V. Correlations between histology and neuronal activity recorded by microelectrodes implanted chronically in the cerebral cortex. *J. Neural Eng.* **13,** 36012 (2016).
19. Wendelken, S. *et al.* Restoration of motor control and proprioceptive and cutaneous sensation in humans with prior upper-limb amputation via multiple Utah Slanted Electrode Arrays (USEAs) implanted in residual peripheral arm nerves. *J. Neuroeng. Rehabil.* **14,** 121 (2017).
20. BeMent, S. L., Wise, K. D., Anderson, D. J., Najafi, K. & Drake, K. L. Solid-state electrodes for multichannel multiplexed intracortical neuronal recording. *Biomed. Eng. IEEE Trans.* **2,** 230–241 (1986).
21. Wise, K. D. *et al.* Microelectrodes, microelectronics, and implantable neural microsystems. *Proc. IEEE* **96,** 1184–1202 (2008).
22. Herwik, S. *et al.* Fabrication technology for silicon-based microprobe arrays used in acute and sub-chronic neural recording. *J. Micromechanics Microengineering* **19,** 074008 (2009).
23. Lopez, C. M. *et al.* A Neural Probe With Up to 966 Electrodes and Up to 384 Configurable Channels in 0.13$\mu $ m SOI CMOS. *IEEE Trans. Biomed. Circuits Syst.* **11,** 510–522 (2017).
24. Cheung, K. C., Djupsund, K., Dan, Y. & Lee, L. P. Implantable multichannel electrode array based on SOI technology. *Microelectromechanical Syst. J.* **12,** 179–184 (2003).
25. Saxena, T. *et al.* The impact of chronic blood-brain barrier breach on intracortical electrode function. *Biomaterials* **34,** 4703–4713 (2013).
26. Boretius, T. *et al.* A transverse intrafascicular multichannel electrode (TIME) to interface with the peripheral nerve. *Biosens. Bioelectron.* **26,** 62–9 (2010).
27. Wurth, S. *et al.* Long-term usability and bio-integration of polyimide-based intra-neural stimulating electrodes. *Biomaterials* **122,** 114–129 (2017).
28. Takeuchi, S., Suzuki, T., Mabuchi, K. & Fujita, H. 3D flexible multichannel neural probe array. *J. micromechanics microengineering* **14,** 104 (2004).
29. Wu, F. *et al.* Silk-backed structural optimization of high-density flexible intracortical neural probes. *J. Microelectromechanical Syst.* (2015). doi:10.1109/JMEMS.2014.2375326
30. Luan, L. *et al.* Ultraflexible nanoelectronic probes form reliable, glial scar–free neural integration.

Sci. Adv. (2017). doi:10.1126/sciadv.1601966

31. Boehler, C. *et al.* Actively controlled release of Dexamethasone from neural microelectrodes in a chronic in vivo study. *Biomaterials* (2017). doi:10.1016/j.biomaterials.2017.03.019
32. Felix, S. H. *et al.* Insertion of Flexible Neural Probes Using Rigid Stiffeners Attached with Biodissolvable Adhesive. *J. Vis. Exp.* 1–12 (2013). doi:10.3791/50609
33. Chung, J. E. *et al.* High-density, long-lating, and multi-region electrophysiological recordings using polymer electrode arrays. *bioRxiv* 242693 (2018).
34. Auciello, O. & Sumant, A. V. Status review of the science and technology of ultrananocrystalline diamond (UNCD^{TM}) films and application to multifunctional devices. *Diam. Relat. Mater.* **19,** 699–718 (2010).
35. Auciello, O. *et al.* Biocompatible ultrananocrystalline diamond coatings for implantable medical devices. *MRS Bull.* **39,** 621–629 (2014).
36. https://physiology.arizona.edu/people/secomb/network/brain99.
37. Buzsáki, G. *et al.* Tools for probing local circuits: High-density silicon probes combined with optogenetics. *Neuron* **86,** 92–105 (2015).
38. Eckert, M., Neyts, E. & Bogaerts, A. Molecular Dynamics Simulations of the Sticking and Etch Behavior of Various Growth Species of (Ultra)Nanocrystalline Diamond Films. *Chem. Vap. Depos.* (2008). doi:10.1002/cvde.200706657
39. Espinosa, H. D. & Peng, B. A new methodology to investigate fracture toughness of freestanding MEMS and advanced materials in thin film form. *J. Microelectromechanical Syst.* (2005). doi:10.1109/JMEMS.2004.839013
40. Moldovan, N., Zeng, H., Carlisle, J. A. & Divan, R. Advanced Diamond Technologies, Inc. (2010).
41. Johnston, I. D., McCluskey, D. K., Tan, C. K. L. & Tracey, M. C. Mechanical characterization of bulk Sylgard 184 for microfluidics and microengineering. *J. Micromechanics Microengineering* **24,** (2014).
42. Subbaroyan, J. & Kipke, D. R. Chronic injury response evoked by intracortical microelectrodes in different tethering modalities. 1–33
43. Gefen, A., Gefen, N., Zhu, Q., Raghupathi, R. & Margulies, S. S. Age-dependent changes in material properties of the brain and braincase of the rat. *J. Neurotrauma* **20,** 1163–1177 (2003).
44. Okamura, A. M., Simone, C. & O'leary, M. D. Force modeling for needle insertion into soft tissue. *IEEE Trans. Biomed. Eng.* **51,** 1707–1716 (2004).
45. Casanova, F., Carney, P. R. & Sarntinoranont, M. In vivo evaluation of needle force and friction stress during insertion at varying insertion speed into the brain. *J. Neurosci. Methods* **237,** 79–89 (2014).
46. Kong, X. Q. & Wu, C. W. Mosquito proboscis: An elegant biomicroelectromechanical system. *Phys. Rev. E - Stat. Nonlinear, Soft Matter Phys.* **82,** 1–5 (2010).
47. Yang, M. & Zahn, J. D. Microneedle Insertion Force Reduction Using Vibratory Actuation. *Biomed. Microdevices* **6,** 177–182 (2004).
48. Römgens, A. M., Bader, D. L., Bouwstra, J. A., Baaijens, F. P. T. & Oomens, C. W. J. Monitoring the penetration process of single microneedles with varying tip diameters. *J. Mech. Behav. Biomed. Mater.* **40,** 397–405 (2014).
49. Nicolelis, M. A. L. *et al.* Chronic, multisite, multielectrode recordings in macaque monkeys. *Proc. Natl. Acad. Sci.* **100,** 11041–11046 (2003).
50. Bjornsson, C. S. *et al.* Effects of insertion conditions on tissue strain and vascular damage during neuroprosthetic device insertion. *J. Neural Eng.* **3,** 196 (2006).

656 51. Sperry, Z. J. *et al.* Flexible microelectrode array for interfacing with the surface of neural ganglia.
657 *J. Neural Eng.* **15,** (2018).
658 52. Rubehn, B. & Stieglitz, T. In vitro evaluation of the long-term stability of polyimide as a material
659 for neural implants. *Biomaterials* **31,** 3449–3458 (2010).
660 53. Ordonez, J., Schuettler, M., Boehler, C., Boretius, T. & Stieglitz, T. Thin films and microelectrode
661 arrays for neuroprosthetics. *MRS Bull.* **37,** 590–598 (2012).
662 54. Patel, P. R. *et al.* Chronic in vivo stability assessment of carbon fiber microelectrode arrays. *J.*
663 *Neural Eng.* **13,** 66002 (2016).
664 55. Stieglitz, T., Beutel, H. & Meyer, J. U. 'Microflex' - A new assembling technique for
665 interconnects. *J. Intell. Mater. Syst. Struct.* **11,** 417–425 (2000).
666 56. Khurram, A. *et al.* Chronic monitoring of lower urinary tract activity via a sacral dorsal root
667 ganglia interface. *J. Neural Eng.* (2017). doi:10.1088/1741-2552/aa6801
668 57. Kadir, S. N., Goodman, D. F. M. & Harris, K. D. High-Dimensional Cluster Analysis with the
669 Masked EM Algorithm. *Neural Comput.* **26,** 2379–2394 (2014).
670 58. Rossant, C. *et al.* Spike sorting for large, dense electrode arrays. *Nat. Neurosci.* **19,** 634–641
671 (2016).

Supplemental Information

Table of Contents

Supplemental Note 1: Mounting polymer arrays to the shuttle
Supplementary Figure 1: Simulation of blood vessel invasion based on various probe cross-sections
Supplemental Note 2: Limits to conformal trench filling with UNCD
Supplemental Figure 2: Simulation result of UNCD profile modeling
Supplementary Figure 3: Measurement setup and force-distance curve for insertion through phantom
Supplementary Figure 4: Phantom insertion force of 1,2,4 and 24 shanks for UNCD
Supplementary Figure 5: Maximum compression distance of UNCD shuttle with varying oscillation frequency at 2 mm/s in tissue phantom
Supplementary Figure 6: Kinematics of instantaneous insertion speed using a piezostage motor with uniaxial motion
Supplementary Table 1: Peak velocity and acceleration of all phantom conditions tested
Supplementary Figure 7: Oscillation and force testing of a 2-µm tip pipette at low speeds in tissue phantom
Supplementary Figure 8: Picture and impedance of PEDOT:pTS coated electrodes
Supplementary Note 3: Detailed results of feline in-vivo experiments
Supplementary Figure 9: Recorded neural signal from somatosensory cortex of rat
Supplementary Video 1: Example of insertion failure due to tissue movement during ex-vivo trial.
Supplementary Video 2: Side-by-side comparison of UNCD insertion without and with 200 Hz oscillation.
Supplementary Video 3: In vivo insertion through rat dura and retraction leaving flexible array implanted
References

696 **Supplemental Note 1: Mounting polymer arrays to the shuttle**

697 Regarding the temporary adhesion of a polymer array onto the diamond shuttle, we describe our
698 PEG mounting process below. The dissolution rate of PEG has to be carefully controlled so that the array
699 doesn't separate prematurely during insertion and the dissolution and separation happens within a
700 reasonable time after insertion. For cat DRG, this is not trivial because there are several hundred microns
701 of relative DRG position shifting as the vertebral region is coupled to the body's movement during
702 breathing. This movement is enough to either cause damage to the tissue or fracture the shuttle. We found
703 that if the UNCD shuttle is removed within five minutes of insertion it did not break in three of three
704 attempts. When left for longer, the shuttle fractured. Comparatively, a head-fixed rat surgery had no time
705 limit and movement was hardly visible(Supplementary Video 3), although Gilletti et. al found this to be
706 around 10-30 μm and varied with anesthesia[1]. We tested the molecular weight of PEG (4,000, 8,000, and
707 12,000 MW) and found the best result for our purposes to be dip coating with 12,000 MW. For rapid
708 removal, using the T-UNCD as a micropost is expected to be as effective as other microposts[2,3] except it
709 would also be stiffer and/or smaller.

710
711
712
713

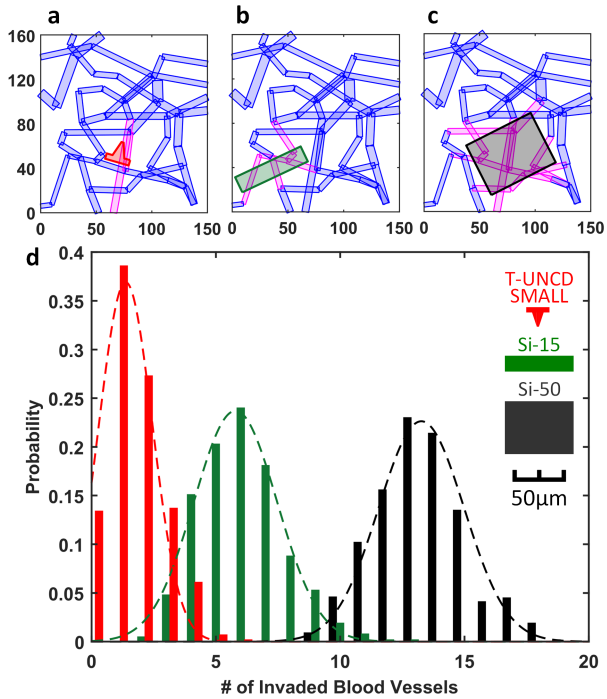

Supplementary Figure 1 | Simulation of blood vessel invasion based on various probe cross-sections. Examples of invasion analysis with **a,** T shape with 22 x 5 µm on the planar portion and 13.5µm-deep, 11 to 2µm-wide trapezoid for the vertical support (red, T-UNCD SMALL). **b,** 65µm by 15µm rectangle (green, Si-15). **c,** 65µm by 50µm rectangle(black, Si-50). **d,** Simulation of 1,000 insertions result in a Gaussian distribution of the numbers of invaded blood vessels. Mean values of three geometries from (a-c) were 1.4, 5.8, and 13.3, respectively. Invaded blood vessels in (a-c) indicated in magenta. X and Y labels in (a-c) indicated the coordinates in µm.

Supplemental Note 2: Limits to conformal trench filling with UNCD

The sticking coefficient (η_0) is a property of CVD deposition and is the most important parameter in determining a film's conformation around 3-D structures. η_0 is dependent on pressure, temperature, and the nature of each species, etc. Theoretically, the shape of the trench and the sticking coefficient determine the deposition profile. As mentioned in the Results section, the sticking coefficient of UNCD deposition varies in a large range and was unknown for the system we used at the time of deposition. The challenge of trench filling of UNCD is the moderate conformality of the UNCD film. Our model estimated that γ= 0.079, which is a moderate sticking coefficient[4]. We resolved the issue by creating a tapered trench (lower aspect ratio) but the curved shape of the T-beam also minimizes high-stress points that would exist around a sharp T-beam geometry. Furthermore, characterizing the critical factors

732 contributing to the sticking coefficient is a long experimental process best done when the process is done
733 in-house as opposed to a commercial service.

734 Ganguli et al[5] and Komiyama et al[6] suggested the governing equation of deposition model based
735 on the mass conservation and it was reformulated as shown in (2). It was assumed that the width of trench
736 is constant along with the depth as well as time. The assumptions are inappropriate due to tapered profile
737 and increasing film thickness over time. The derivative equation becomes unsolvable form and analytical
738 solution cannot be derived.

739 $$\frac{d}{dy}\left(\frac{2W^2}{3\eta_0}\frac{dC}{dy}\right) = C \qquad (2)$$

740 where W is the width of trench, η_0 is the sticking coeffieient, and C is the concentration of reactant.

741 Instead, we converted the derivative equation to a discrete form and iterated the calculation
742 according to the depth and the time. The film thickness deposited on discrete coordinates of y during a
743 unit time was calculated with the fixed width and then the width was updated considering the deposited
744 film for the following calculation during the next unit time. The calculation was iterated until the time
745 when the targeted total thickness was achieved.

746 The model predicted a slight hollow in the middle of the trench since the etched profile was not
747 linear and the sidewall angle of some portion was above the critical angle (70˘) for void-free filling even
748 though the averaged angle was more tapered. Since a small void has a small change in the moment of
749 inertia, we also expect a small loss of mechanical strength.

750 Finally, it is noted that the residual stress of UNCD film is not consistent during deposition and
751 the resulting gradient make it challenging to control or compensate for residual stress with a thick film
752 UNCD. The moderate sticking coefficient and stress gradient will eventually limit the aspect ratio and
753 film thickness so the upper limit of strength we estimate to be in the range of 65 gf based on our current

film properties. This is sufficient for all of the animal models for which we currently have data for.

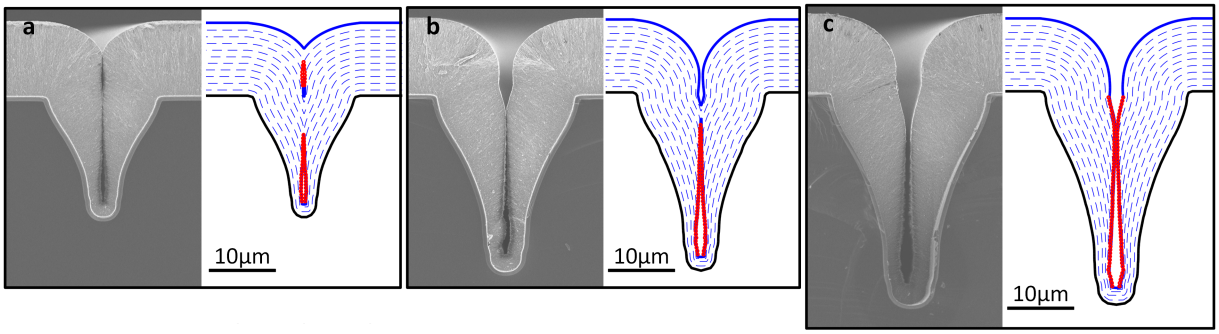

Supplementary Figure 2 | Simulation result of UNCD profile modeling. a, design A with 18.3µm-deep trench, R^2=0.957. **b,** design B with 26.9µm-deep trench, R^2=0.946. **c,** design C with 32.2µm-deep trench, R^2=0.943. Blue solid line is the final outline of UNCD film. Blue dashed lines show the progression of deposition. Red lines indicate the measured profiles of UNCD film.

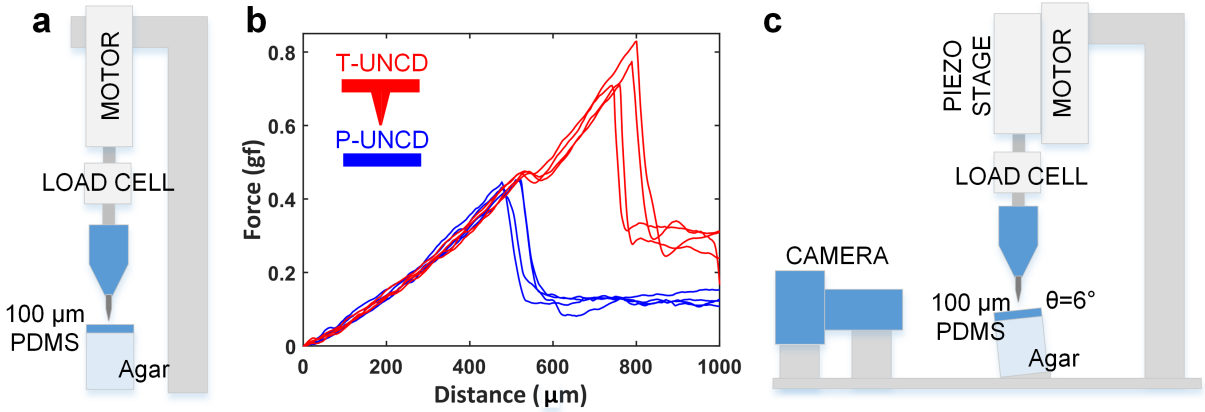

Supplementary Figure 3 | Measurement setup and force-distance curve for insertion through phantom. a, Measurement setup with a motor, a load cell and a tissue phantom with 100µm-thick PDMS. The phantom uses 100-µm thick layer of Sylgard 184 silicone (1-2 MPa[7]) over 0.7% agar to represent a membrane and soft nervous tissue. **b,** Force-distance curve for P- UNCD and T-UNCD. T-UNCD showed two bumps, with the earlier one indicating the insertion of the planar tip. Insertion speed 0.01mm/s and acceleration 0.1mm/s^2. **c**, Measurement setup that includes a camera with 4X macro lens to measure maximum compression distance. Piezomotor from PiezoConcept, Inc designed for high-precision microscope stages was used here to enable uni-axial sinusoidal oscillations of up to 70-µm peak-to-peak.

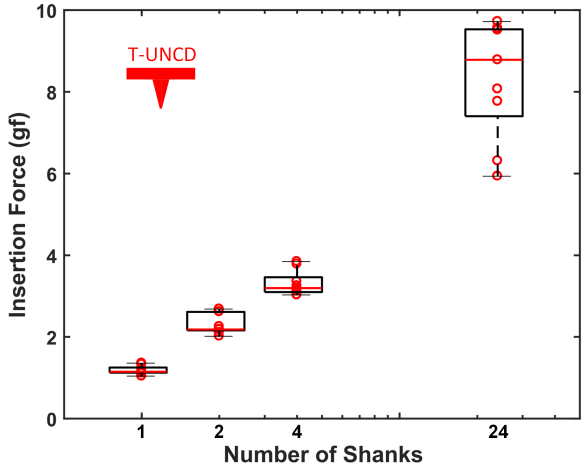

Supplementary Figure 4 | Phantom insertion force of 1,2,4 and 24 shanks for UNCD. To achieve 24 shanks, we arranged six 4-shank arrays in a hexagonal pattern. The force per shank in this case is 0.35 gf, a 66% and 72% force reduction relative to the 4-shank and 1-shank designs (Figure 3). This mechanism of local force reduction is yet unknown and may vary from shank to shank so more research on the local stress may help to reduce the size of a large number of shanks relative to the single shank version.

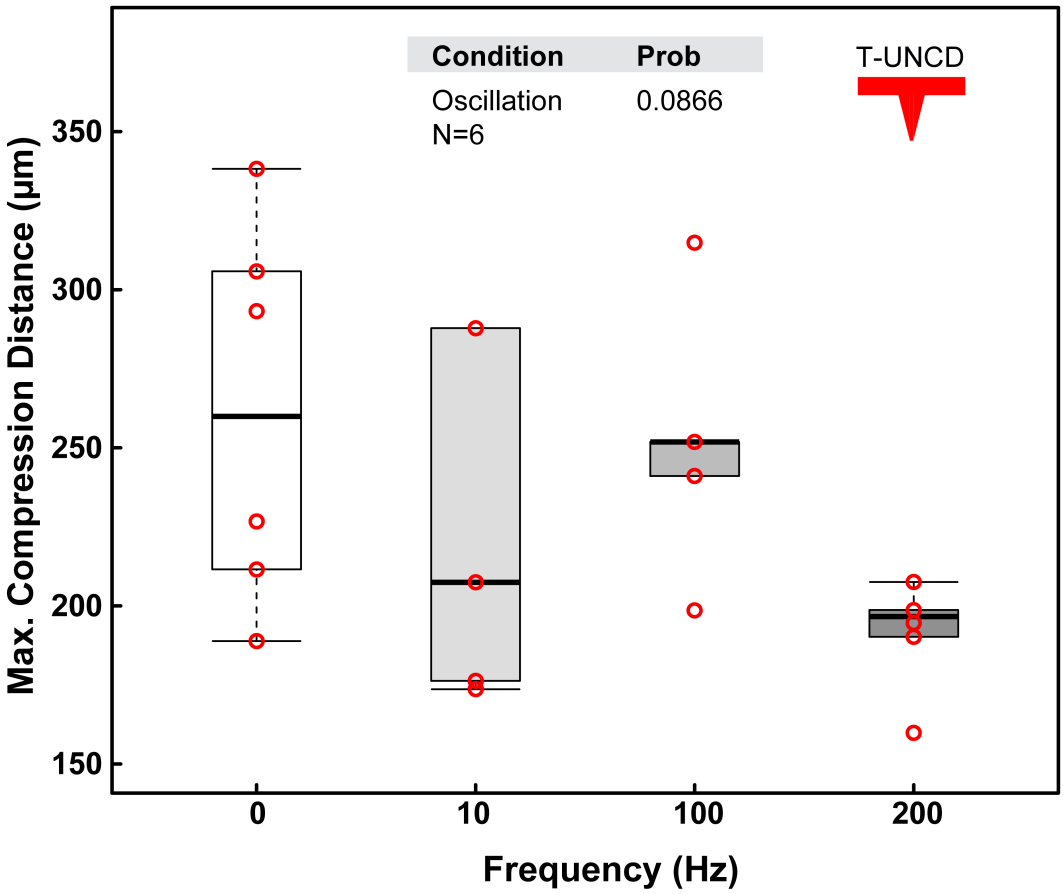

Supplementary Figure 5 | Maximum compression distance of UNCD shuttle with varying oscillation frequency at 2 mm/s in tissue phantom.

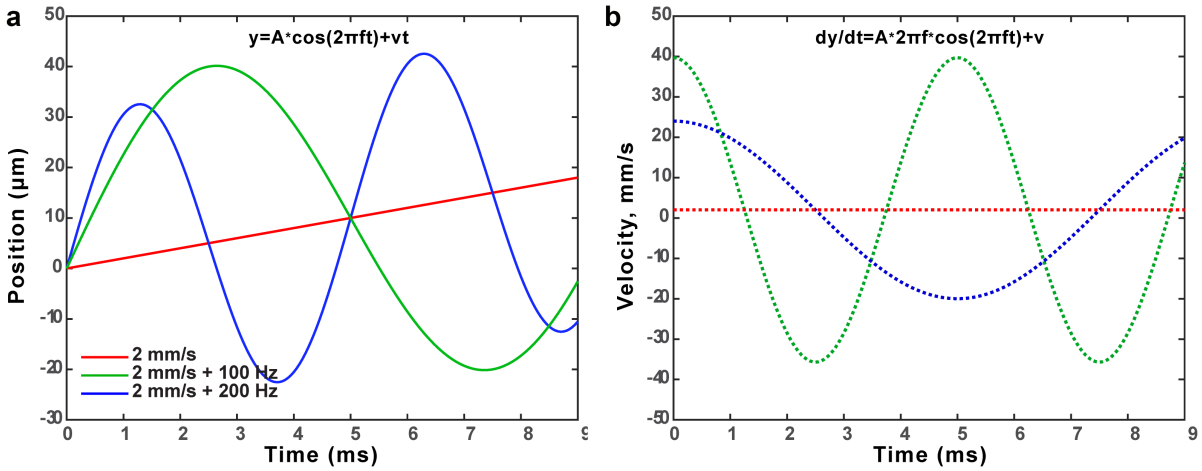

Supplementary Figure 6 | Kinematics of instantaneous insertion speed using a piezostage motor with uniaxial motion. The position equation and its first derivative are defined in the figures where A is maximum amplitude for a given oscillation. Beyond 200 Hz, the amplitude of this piezostage, HS1.70 from PiezoConcept, was dampened (see Supp. Table 1).

Supplementary Table 1 | Peak Velocity and Acceleration of All Phantom Conditions Tested

	Frequency			
	10	**100**	**200**	**400[A]**
Max amplitude (µm)	35	35	30	13.6
Max speed (mm/s)	2.2 + linear sp	22 + linear sp	38 + linear sp	34 + linear sp
Max acceleration (m/s^2)	0.1	14	47	86

Note A: 400 Hz was only tested at 0.01 mm/s and only for 2 trials. Given it was a slower speed than 200 Hz and showed no improvement in those 2 trials we dropped this condition from the study.

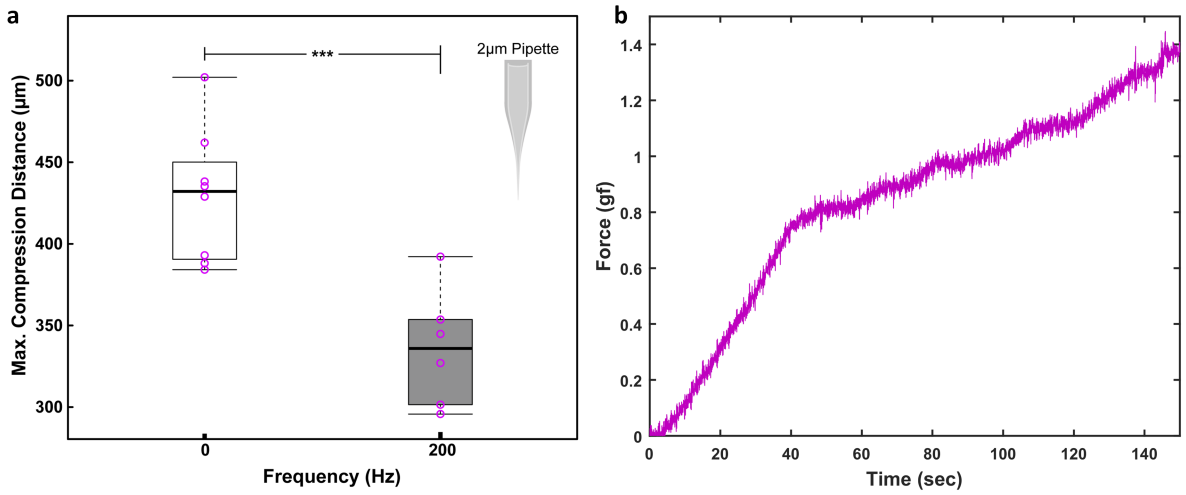

Supplementary Figure 7 | Oscillation and force testing of a 2-µm tip pipette at low speeds in tissue phantom. Glass pipettes are still a common implantable sensor for neuroscience and makes a useful model understanding the effect of device cross-sectional area, which is monotonically increasing. **a,** Oscillation significantly reduces the maximum compression distance (p=0.00074, N>6). **b,** While the tip is very sharp, we observe that the larger cross-sectional area dominates the force response, as reported by others[8].

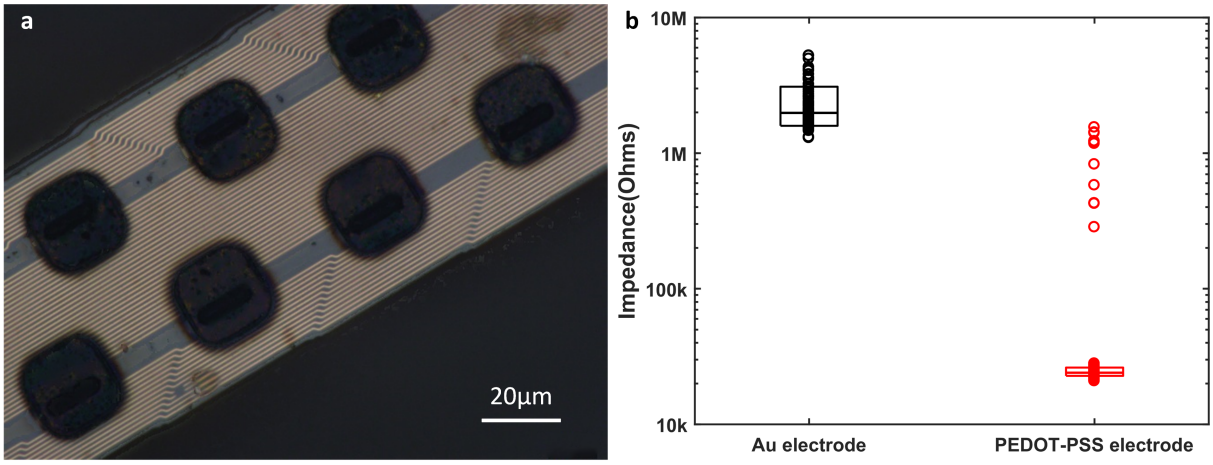

Supplementary Figure 8 | Picture and impedance of PEDOT:pTS coated electrodes. a, Poly(3,4-ethylenedioxythiophene: Sodium p-toluenesulfonate was plated on Au electrodes with a current of 690 nA and duration of 10 minutes as described in Patel, et. al 2016[9]. **b,** Impedances at 1kHz for non-coated Au electrodes and PEDOT-pTS coated electrodes, N=120. Top, middle and bottom lines of box plots indicates 90% value, harmonic mean, and 10% value, respectively. For the PEDOT-pTS coated electrodes, 14 electrodes with relatively high impedance were excluded as outliers.

Supplementary Note 3: Detailed results of feline in-vivo experiments

This note includes additional descriptions of the electrode performance. In the first animal experiment a total of 28 different channels had a unit out of 42 functional channels during six sensory input trials. The per trial average was 11 units across 8 channels with single unit amplitudes between 35-323 µV peak-to-peak (mean 68

μVp-p, median 47 μVp-p).

In the second animal experiment an average of 78 units across 32 channels were observed during each of eight evoked trials during testing with the electrode in a fixed position, with single unit amplitudes between 39-1313 μV peak-to-peak (mean 123 μVp-p, median 80 μVp-p). Across multiple trials in this fixed position, a total of 48 different channels had a unit (167 non-unique units observed) out of 59 functional channels, spanning 1.06 mm in depth. When this same probe was retracted, units clearly moved between electrodes, including appearing on electrodes that were deeper in the tissue, suggesting that the tip of the array may have initially been in an inactive region of the DRG or in the ventral root (Fig. 7a). During movement of the probe, a total of 249 units were identified, with all 59 functional channels having activity across the full 1.2 mm span. Single units during the probe movement trial were within 50-1273 μV peak-to-peak (mean 199 μVp-p, median 125 μVp-p).

As the channels within the electrode array were separated by 40 μm, some units appear on multiple channels and we used careful manual sorting followed by comparison of waveform shapes across neighboring channels to report putative units. High-density arrays, like that used here, are best employed using an unbiased polytrode analysis as others have demonstrated[10–12] to eliminate double counts but also to increase the number of unique identifiable units when performing an in-depth mapping study[13].

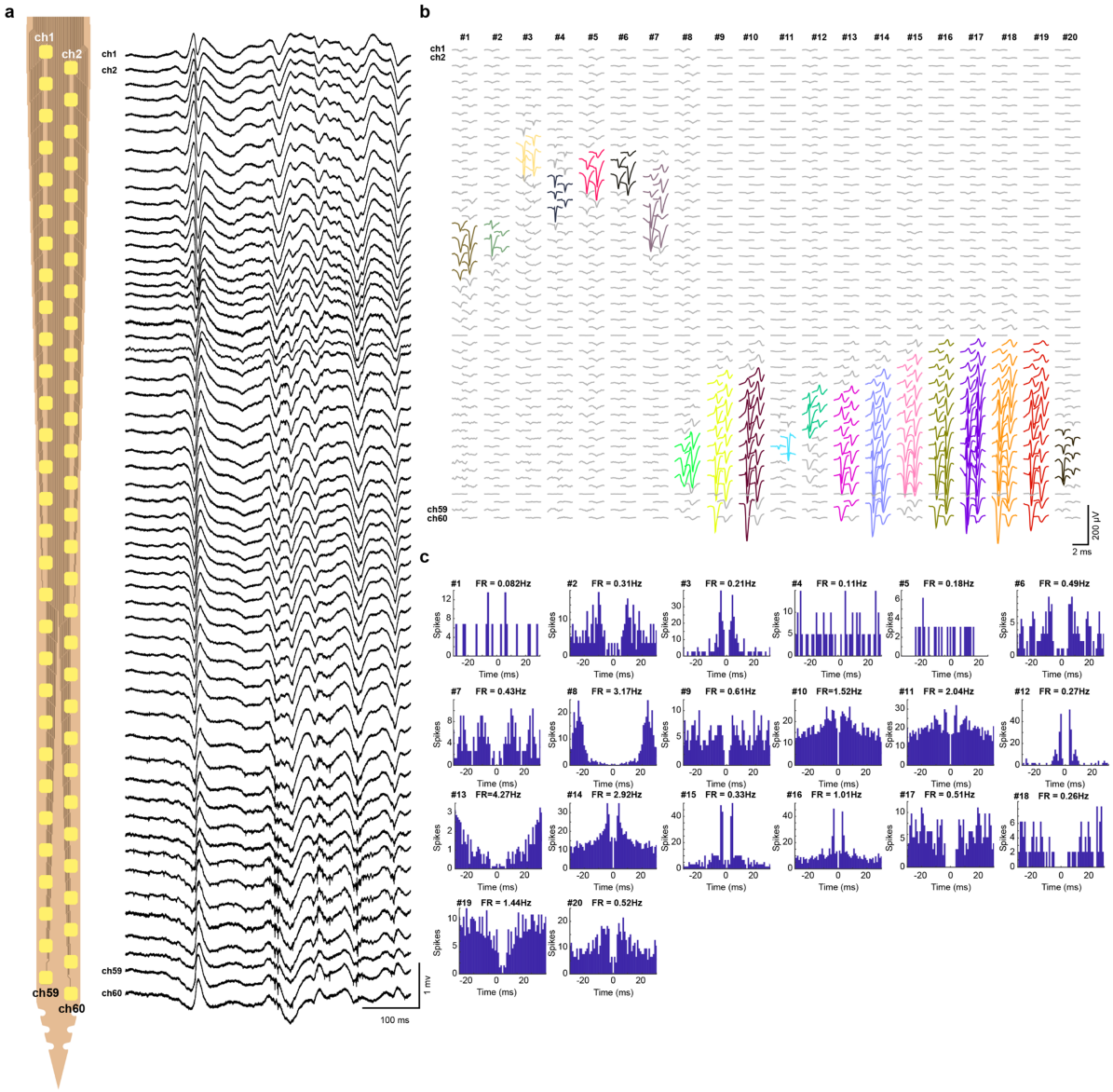

Supplementary Figure 9 | Recorded neural signal from somatosensory cortex of rat. a, Wide-band (0.3 – 3000 Hz) spiking activity recorded on a flexible electrode from S1FL region of an anesthetized rat (right) and a schematic of the probe sites (left). Note the spiking activity at the bottom of the shank. **b,** Recording of high number of well-isolated single units. The spiking data was quantified for 20 putative single units recorded simultaneously from S1FL (same animal and session as in **a**). Plots show average single-unit triggered waveforms (n = number of spikes, at least 500) on all channels. Note the single unit activity is present across multiple channels but the larger than expected range is due to the movement of probe relative to the brain tissue over the course of 30 minutes. **c,** Auto-correlation histograms of the 20 putative single units (same as **b**). Mean firing rate (FR) value is shown for each unit above the histogram.

Supplementary Video 1 | Example of insertion failure due to tissue movement during *ex-vivo* trial. The insertion speed was 0.01mm/sec and the travel distance was 1.5mm. The video showed the buckling failure of P-UNCD during the insertion trial into DRG L7 explanted from a feline. Link for video will be provided in a peer-reviewed journal article.

Supplementary Video 2 | Side-by-side comparison of UNCD insertion without and with 200 Hz oscillation. The linear speed of insertion was 0.01mm/s for both. Link for video will be provided in a peer-reviewed journal article.

Supplementary Video 3 | In vivo insertion through rat dura and retraction leaving flexible array implanted. The polyimide electrode array on T-UNCD shuttle was implanted into the motor cortex and the T-UNCD shuttle was successfully retracted, leaving the polyimide array inside. The insertion was conducted at 0.01mm/s speed with 200Hz oscillation. Retraction occurred in steps of 50 to 100 µm to ensure separation was visible before larger movements were made. Link for video will be provided in a peer-reviewed journal article.

References:

1. Gilletti, A. & Muthuswamy, J. Brain micromotion around implants in the rodent somatosensory cortex. *J. Neural Eng.* **3,** 189 (2006).
2. Luan, L. *et al.* Ultraflexible nanoelectronic probes form reliable, glial scar–free neural integration. *Sci. Adv.* (2017). doi:10.1126/sciadv.1601966
3. Boehler, C. *et al.* Actively controlled release of Dexamethasone from neural microelectrodes in a chronic in vivo study. *Biomaterials* (2017). doi:10.1016/j.biomaterials.2017.03.019
4. Eckert, M., Neyts, E. & Bogaerts, A. Molecular Dynamics Simulations of the Sticking and Etch Behavior of Various Growth Species of (Ultra)Nanocrystalline Diamond Films. *Chem. Vap. Depos.* (2008). doi:10.1002/cvde.200706657
5. Ganguli, S., Costello, S. P. & Gill, W. N. Theory of Free Boundary Step Coverage in Chemical Vapor Deposition. *Ind. Eng. Chem. Res* **34,** 3380–3391 (1996).
6. Komiyama, H., Shimogaki, Y. & Egashira, Y. Chemical reaction engineering in the design of CVD reactors. *Chem. Eng. Sci.* **54,** 1941–1957 (1999).
7. Johnston, I. D., McCluskey, D. K., Tan, C. K. L. & Tracey, M. C. Mechanical characterization of bulk Sylgard 184 for microfluidics and microengineering. *J. Micromechanics Microengineering* **24,** (2014).
8. Römgens, A. M., Bader, D. L., Bouwstra, J. A., Baaijens, F. P. T. & Oomens, C. W. J. Monitoring the penetration process of single microneedles with varying tip diameters. *J. Mech. Behav. Biomed. Mater.* **40,** 397–405 (2014).
9. Patel, P. R. *et al.* Chronic in vivo stability assessment of carbon fiber microelectrode arrays. *J. Neural Eng.* **13,** 66002 (2016).
10. Rossant, C., Kadir, S. & Harris, K. Spike sorting for large dense electrode arrays: User interface software. *Annu. Meet. Soc. Neurosci.* (2013).
11. Chung, J. E. *et al.* A Fully Automated Approach to Spike Sorting. *Neuron* **95,** 1381–1394.e6 (2017).
12. Jun, J. J. *et al.* Real-time spike sorting platform for high-density extracellular probes with ground-truth validation and drift correction. *bioRxiv* 1–29 (2017). doi:https://doi.org/10.1101/101030
13. Gray, C. M., Maldonado, P. E., Wilson, M. & McNaughton, B. Tetrodes markedly improve the reliability and yield of multiple single-unit isolation from multi-unit recordings in cat striate cortex. *J. Neurosci. Methods* **63,** 43–54 (1995).